BIOMIMETICS

Insect-scale fast moving and ultrarobust soft robot

Yichuan Wu[1,2,3], Justin K. Yim[4], Jiaming Liang[1,2,3], Zhichun Shao[2,3], Mingjing Qi[2,3,5], Junwen Zhong[2,3]*, Zihao Luo[2], Xiaojun Yan[5], Min Zhang[6]*, Xiaohao Wang[1,6], Ronald S. Fearing[4], Robert J. Full[4,7], Liwei Lin[1,2,3]*

Mobility and robustness are two important features for practical applications of robots. Soft robots made of polymeric materials have the potential to achieve both attributes simultaneously. Inspired by nature, this research presents soft robots based on a curved unimorph piezoelectric structure whose relative speed of 20 body lengths per second is the fastest measured among published artificial insect-scale robots. The soft robot uses several principles of animal locomotion, can carry loads, climb slopes, and has the sturdiness of cockroaches. After withstanding the weight of an adult footstep, which is about 1 million times heavier than that of the robot, the system survived and continued to move afterward. The relatively fast locomotion and robustness are attributed to the curved unimorph piezoelectric structure with large amplitude vibration, which advances beyond other methods. The design principle, driving mechanism, and operating characteristics can be further optimized and extended for improved performances, as well as used for other flexible devices.

INTRODUCTION

Mobility and robustness are two engineering challenges for robots. Unlike large-scale robots based on materials of high stiffness/density and powered by bulky actuators/motors, small-scale soft robots are often restricted to small actuators with low output power based on materials of low stiffness/density. Hence, insect-scale soft robots are known to be easily damaged, exhibit poor control of locomotion, or are slow moving due to the nature of their small structures. Improving the mobility, efficiency, and robustness of soft robots made of a deformable body with the capability to carry extra weights to perform various functions has been challenging (1–4). Researchers have tried to develop soft robots that negotiate complex environments by taking advantage of soft matter physics in the interdisciplinary field termed "robophysics" (5, 6). Recent advances include micro/millimeter-scale robots with good mobility, such as crawling robots (7–11), hopping robots (12, 13), and multi-legged robots (14–18). However, these robots are made of rigid or partially rigid parts, resulting in poor robustness and low adaptability to shape changes and/or external perturbations. On the other hand, soft robots actuated by humidity (19–21), light (22–24), heat (25), and magnetic force (26–28) have been demonstrated but have slow responses, whereas others require bulky setups to generate the external power sources such as magnetic fields. Robots using thin film–based actuators based on lead zirconate titanate (PZT) have been successfully developed (17, 18, 29–31), but PZT is a brittle material containing poisonous lead. Polyvinylidene difluoride (PVDF) is soft, flexible, and lightweight, making it suitable for potential soft robot applications (32, 33), but one key challenge has been to generate fast, effective movement and even locomotion (34).

The locomotion mechanisms of animals continue to inspire the design of soft robots (4, 35). In particular, arthropods show how rapid, cyclic locomotion at high frequencies at this scale is possible without compromising robustness and survivability in harsh conditions (36, 37). Flying mosquitos can oscillate or vibrate their wings at more than 800 Hz (38), and 1-mm mites attain relative ground speeds exceeding 200 body lengths per second (BL/s) (39, 40). In this work, we introduce fast and robust insect-scale soft robots based on a curved piezoelectric PVDF unimorph structure to achieve several key advancements: (i) Under an alternating current (AC) driving power near the resonant frequency (850 Hz) of the structure, a prototype 10-mm-long robot (0.024 g) attained a relative speed of 20 BL/s—the fastest among published reports of insect-scale soft ground robots; (ii) after stepping on the robot with an adult human's full body weight (59.5 kg, about 1 million times heavier than the robot), the robot could still move afterward, demonstrating exceptional robustness; (iii) the robot could move smoothly carrying a load weighing 0.406 g, which is six times heavier than that of the robot; (iv) further enhancement of agility was demonstrated by designing the moving mechanism to emulate features of galloping-like gaits using a two-leg prototype robot.

RESULTS

Structure and working mechanism

A prototype 3 cm–by–1.5 cm robot, consisting of a curved body and a leg-like structure at the front, is pictured alongside a U.S. quarter in Fig. 1A. A cross-sectional view scanning electron microscopy (SEM) image shows the unimorph structure made of an 18-μm-thick PVDF layer, two 50-nm-thick palladium (Pd)/gold (Au) electrodes (top and bottom of the PVDF film), a 25-μm-thick adhesive silicone, and a 25-μm-thick polyethylene terephthalate (PET) substrate at the bottom. The PVDF layer can produce periodic extension and contraction by the piezoelectric effect under an AC driving voltage to change the shape of the robot; the details of the actuation mechanism are explained in section S1 and fig. S1. This results in an oscillatory center of mass (COM) trajectory pattern (see movie S1) similar to many running animals (36). Figure 1B compares the COM motion of a cockroach and our prototype robot. Although the robot

[1]Tsinghua-Berkeley Shenzhen Institute, Tsinghua University, Shenzhen 518055, China. [2]Berkeley Sensor and Actuator Center, University of California at Berkeley, Berkeley, CA 94720, USA. [3]Department of Mechanical Engineering, University of California at Berkeley, Berkeley, CA 94720, USA. [4]Department of Electrical Engineering and Computer Science, University of California at Berkeley, Berkeley, CA 94720, USA. [5]School of Energy and Power Engineering, Beihang University, Beijing 100191, China. [6]Graduate School at Shenzhen, Tsinghua University, Shenzhen 518055, China. [7]Department of Integrative Biology, University of California at Berkeley, Berkeley, CA 94720, USA.
*Corresponding author: junwenzhong@berkeley.edu (J.Z.); zhang.min@sz.tsinghua.edu.cn (M.Z.); lwlin@berkeley.edu (L.L.)
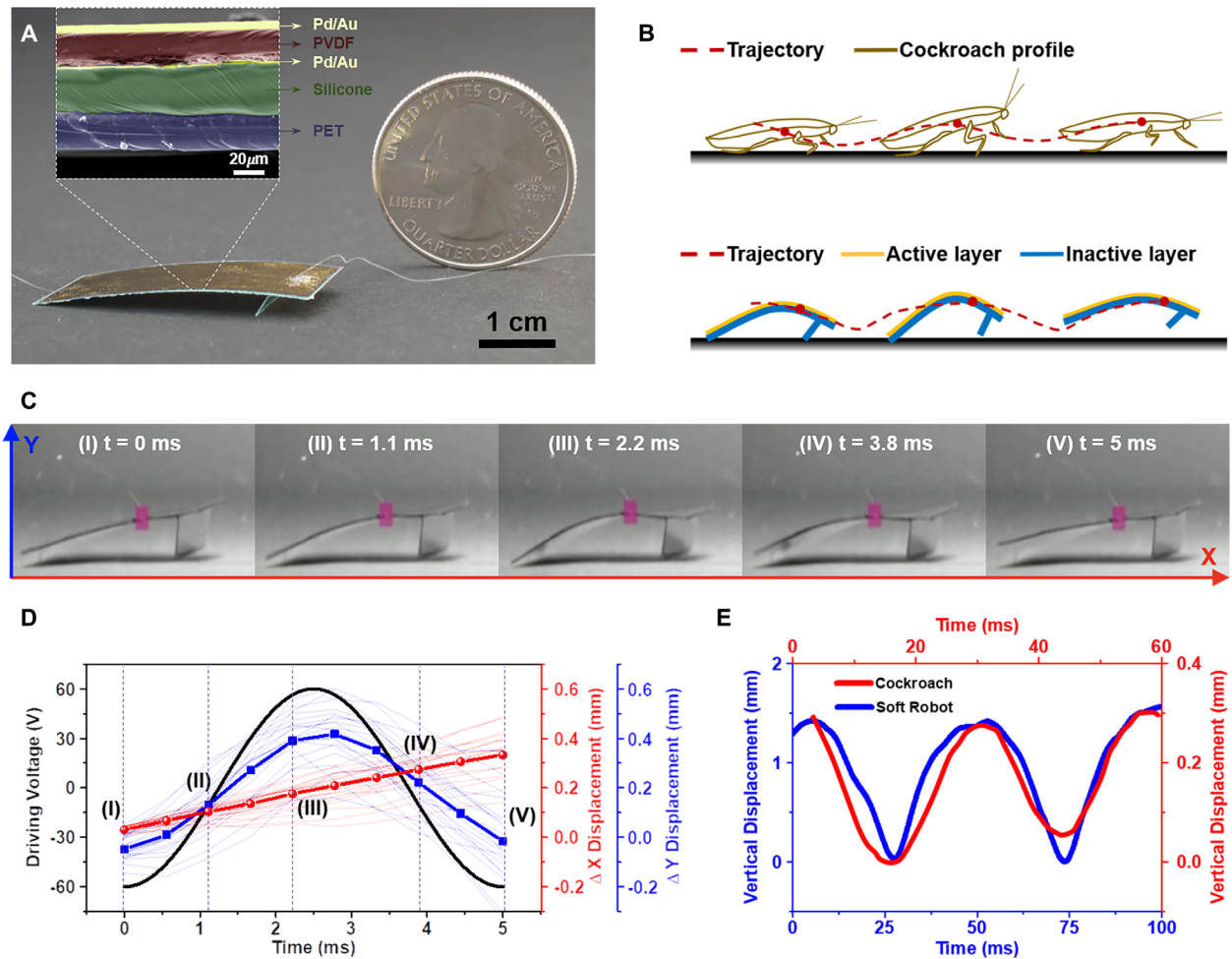
Fig. 1. The prototype and working mechanism. (**A**) Optical photo showing a robot connected with two electrical wires to the top and bottom electrodes, respectively, alongside a U.S. quarter coin. The inset SEM image shows the cross-sectional view of the prototype robot with different layers of materials. (**B**) Comparison of the wavelike running paths showing the movements of the COM of a cockroach (*41*) and a prototype robot (from movie S1). (**C**) Series of optical images recording the movements of a prototype robot in one driving cycle. (**D**) Applied driving signal (black line) and vertical (blue lines) and lateral displacements (red lines) of a prototype robot, where the bold solid lines are the average movements for 20 cycles. (**E**) Two-step cycles of the vertical displacement of the COM during cockroach running [red line for a period of 60 ms, (*41*)] compared with a prototype soft robot (blue line for a period of 100 ms).

has a unique morphology compared with many animals, it also showed a wavelike path. We developed a two-segment mass-spring model to best predict the robot's dynamic movements.

High-speed videos (sampling rate of 2000 frames per second) with a sequence of optical images in Fig. 1C have been used to record the postures and positions of the prototype robots (under −60 to 60 V of sinusoidal driving voltage at 200 Hz, which generates nonmaximal running performance; movie S2) running on a standard printing paper substrate. Within one cycle of the applied sinusoidal voltage, one set of the corresponding successive postures is depicted as states (I) to (V) in Fig. 1C as an example. In state (I) under −60 V, the body is extended and the front leg of the robot is in the ground-touching posture, whereas the abdomen is in the aerial posture. After 1.1 ms at state (II) under an applied voltage close to 0 V, the body recovers its initial shape, whereas the front leg of the robot is still in the ground-touching posture and the abdomen is in the aerial posture with a shorter distance to the ground as compared with that in state (I). In state (III) under +60 V, the body is contracted, and both the front leg and abdomen of

the robot are in the ground-touching posture. In the first-half driving cycle from state (I) to state (III), the body transitions from extended near-flat shape, to the initially curved shape, and then to the contracted shape. These shape changes cause the front leg to strike against the ground and produce a forward-pushing ground reaction force. In the second-half driving cycle from state (III) to state (V), the body goes through the similar shape changes, with the reverse order from the contracted shape to near-flat shape, which could cause the front leg to produce a backward-pushing ground reaction force to slow down the forward moving speed of the robot. Hence, we designed the bending angle of the front leg to be less than 90° to enhance the forward movements and reduce backward movements. Driven under high-frequency actuation coupled with various ground impact conditions and manufacturing variations, the exact shape changes and movements of the robot are rather complex. However, by varying design and operation parameters, the forward moving speed of the robot could be optimized. For example, Fig. 1D shows the experimental results of the lateral displacement (red lines) and vertical displacement

(blue lines) of a prototype robot under a driving voltage between −60 and 60 V (black line). In this analysis, the lateral/vertical displacement is defined as the lateral/vertical movements of the COM of the robot with respect to the original position. The randomness of the individual cycle is clearly observed in both displacements, although the average vertical COM positions follow the driving patterns and the average lateral COM positions show incremental forward movement.

Figure 1E compares two-step cycles of the vertical movement of a cockroach (*41*) and the prototype soft robot (movie S1) with respect to time.

Animals appear to use resonant frequencies to oscillate their muscles and segments (*42*), with the flight muscles and thorax of flying insects serving as an example in the higher frequency range (*43*). We found that it was also desirable to drive the prototype robots near their resonant frequencies for largest deformations. To constrain the running direction of the robot so as to characterize their relative running speed, we used a transparent quartz tube with an inner diameter of 1 inch, as shown in fig. S2 (A and B). In this case, a 10-mm-long prototype (0.024 g) robot was used to achieve a relative running speed up to 20 BL/s driven near its resonant frequency at 850 Hz. In comparison, under driving frequencies of 800 and 900 Hz, lower relative running speeds of 13 and 3.6 BL/s were recorded, respectively (movie S3).

Locomotion analysis

We observed four main postures during the operation of the robot: aerial, front-touching, back-touching, and both-touching. In each posture, the robot's body can be either expanding or contracting depending on the applied driving signal at that instant. Hence, there are eight possible configurations, as shown in Fig. 2 (A to D), where gray dashed lines indicate the previous shapes and red solid lines are the immediate current shapes. In this illustration, G, F_f, and F_a are the gravitational force, ground reaction force at the end of the abdomen, respectively. The shape of the robot changes periodically based on the PVDF actuation force to excite elastic oscillations for the curved unimorph structure. The directions of the ground reaction force at the front leg and abdomen (blue arrows in the figure) will change depending on the posture and shape changes of the robot. The front leg construction of the robot is important because it produces
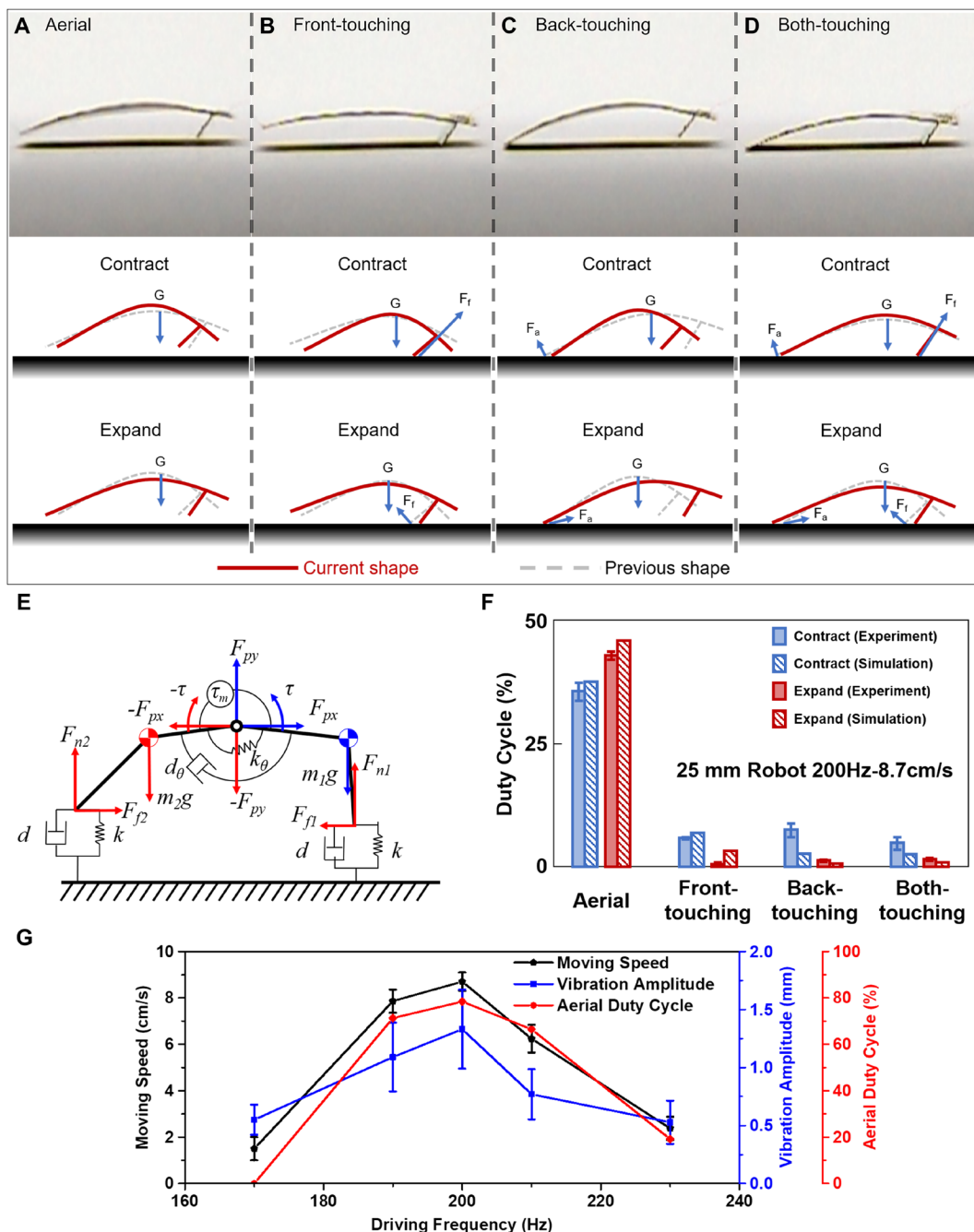

Fig. 2. Locomotion gait analysis. (**A** to **D**) Optical photos from the high-speed camera (top), corresponding contracted configurations (middle), and corresponding expanded configurations (bottom) of a prototype robot showing different gaits in the cross-sectional views. (**E**) Simplified dynamic model based on two rigid bodies joined by a pin joint (both-touching posture as an example) with a torsional spring-damper system. (**F**) Duty cycles in different gaits of both experimental and simulation results for a 25-mm-long prototype robot driven at its fastest speed at resonance of 200 Hz. (**G**) Relationships between the vibration amplitude and moving speed as well as aerial duty cycle for driving frequencies of 170, 190, 200, 210, and 230 Hz. Error bars indicate mean ± 1 SD.
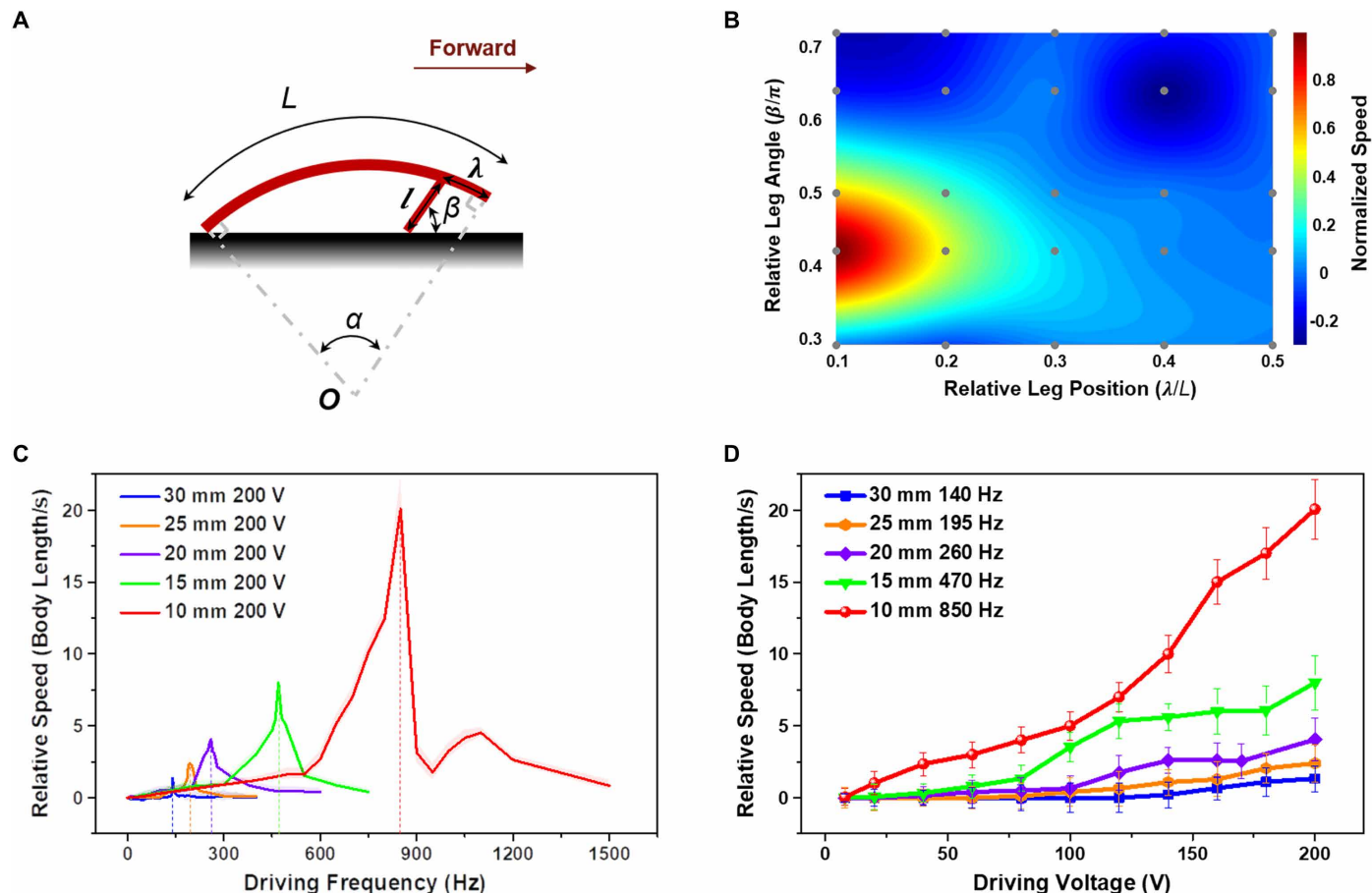
Fig. 3. Geometric parameter optimization and performance characterization. (**A**) Side view of a robot with the definitions of geometric parameters. (**B**) Experimental results (gray dots) for normalized running speeds from a 10-mm-long robot with different geometric combinations used to plot a color map as a function of relative leg position (λ/L) and relative leg angle (β/π). The color map is interpolated by the thin-plate spline interpolation scheme for surface fitting. Original data can be found in table S2. (**C**) Relative running speeds of robots versus the driving frequencies for robots with lengths of 10, 15, 20, 25, and 30 mm. Shaded bands represent 90% confidence limits. (**D**) Relative running speeds (under the resonant frequency) of robots versus the driving voltages for robots with lengths of 10, 15, 20, 25, and 30 mm. Error bars indicate mean ± 1 SD.

anisotropic lateral forces to generate forward locomotion. The most effective configuration for forward motion, a contracting touchdown of the front leg (contraction of the front-touching posture), greatly increased the lateral component of the ground reaction force and the vertical component for taking off. The abdomen functions to keep the balance of the dynamic system by adjusting the pitch of the body when it taps the ground, preventing the robot from flipping over backward. The details for qualitative introduction of the locomotion mechanism are discussed in section S2 and figs. S3 and S4.

Using a high-speed camera, we found that the first vibrational mode is easily excited and dominates the shape change, whereas higher-order modes can be neglected. A dynamic mass-spring model consisting of two rigid bodies (m_1, m_2) joined by a pin joint was analyzed in MATLAB to model the curved robot, as shown in Fig. 2E (both-touching posture as an example). A torsional spring-damper (k_θ-d_θ) at the pin joint is excited by a sinusoidally varying torque source (τ_m) to represent the mechanical motions of the PVDF layer under the AC excitation. We modeled the ground contact at the front and back as a vertical spring-damper (k-d) with a normal force in the vertical direction (F_n) and a friction force in the lateral direction (F_f). The values of material parameters used in the model

and simulation can be found in table S1, and the simulation details are discussed in section S3 and fig. S5.

A 25-mm-long prototype robot was driven on a paper substrate and recorded under different driving parameters. The fastest running speed was 8.7 cm/s (movie S1) under 200 V at 200 Hz. The running speed reduced under the same applied voltage of 200 V at varying frequencies of 170, 190, 210, and 230 Hz, respectively (movie S4). To further study the operation of the robot, we statistically characterized the duty cycles for the eight configurations (Fig. 2, A to D). We plotted the results in Fig. 2F (shaded columns) for the trial with the fastest speed at 8.7 cm/s at 200 Hz (see fig. S6 for other frequencies with slower speeds). We also compared these results with the simulation data from the mass-spring model running at 200 Hz (Fig. 2F, hatched columns, and movie S5). We observed that a large percentage of aerial duty cycles were required to generate fast running speeds for the robot. For example, in this trial, the aerial cycles for the contracted and expanded configurations are about 36 and 43%, respectively, whereas all the other configurations have the duty cycles of less than 10%. In principle, large-amplitude oscillation driven at the resonant frequency should result in large deformation and greater forces to induce longer aerial duty cycles and higher foot velocities for faster speeds. Figure 2G compares the

average vibration amplitudes (measured when the robot is in the aerial posture) under the driving frequencies of 170, 190, 200, 210, and 230 Hz and their corresponding running speeds and aerial duty cycles. As expected, the large vibration amplitude due to the structural resonance resulted in faster running speed as well as longer aerial duty cycles (the combination of contracted and expended configurations). Again, we note that although the morphology and motion of our robot do not mimic any specific animal, small runners, such as cockroaches (41) and desert ants (44), also use aerial phases to attain their fastest speeds.

Parameter optimization and performance characterization

Geometric parameters play an important role in the performance of the robot. To simplify the structure and identify appropriate configurations, we defined the geometric parameters as shown schematically in Fig. 3A, where L is the body length of a robot, α is the body curvature, l is the length of the front leg, λ is the distance between the front leg and the head, and β is the contact angle between the front leg and the ground. Using a prototype robot of 10 mm (length) by 15 mm (width) by 3 mm (height) as an example, we first selected 25 combinations (Fig. 3B, gray dots) of the above geometric parameters to fabricate prototypes and conducted experiments to plot the normalized running speed map as a function of relative leg position (λ/L) and relative leg angle (β/π) in Fig. 3B. The color bar shows the magnitudes and directions of the normalized speed of the robot, with the red color areas representing the fastest running speed. We found that the values of λ/L and β/π near 0.1 and 0.4, respectively, resulted in robots with the fastest running speeds.

We then fabricated prototype robots with different lengths ranging from 10 to 30 mm at an interval of 5 mm using the map of λ/L and β/π of 0.1 and 0.4 for guidance. The resonant frequencies of robots with different lengths were approximately evaluated both analytically and experimentally and discussed in section S4 and figs. S7 and S8. In general, robots with smaller lengths have higher resonant frequencies and faster relative speeds. The relationships between driving frequency and relative speed for robots with lengths of 10, 15, 20, 25, and 30 mm are shown in Fig. 3C driven by a peak-to-peak voltage of 200 V to achieve measured maximum speeds of 20 BL/s (20 cm/s), 8 BL/s (12 cm/s), 4.05 BL/s (8.1 cm/s), 2.4 BL/s (6 cm/s), and 1.33 BL/s (4 cm/s), respectively. In Fig. 3D, the amplitude of the driving voltage versus the relative speed of robots with different lengths was measured near their resonant frequencies. As expected, larger driving voltages result in faster running speeds. For a 10-mm-long robot, as shown in fig. S9 (A and B), we observed noticeable motion even under an AC drive voltage as low as 8 V peak to peak (movie S6), which is a relatively low voltage requirement among insect-scale piezoelectric actuators
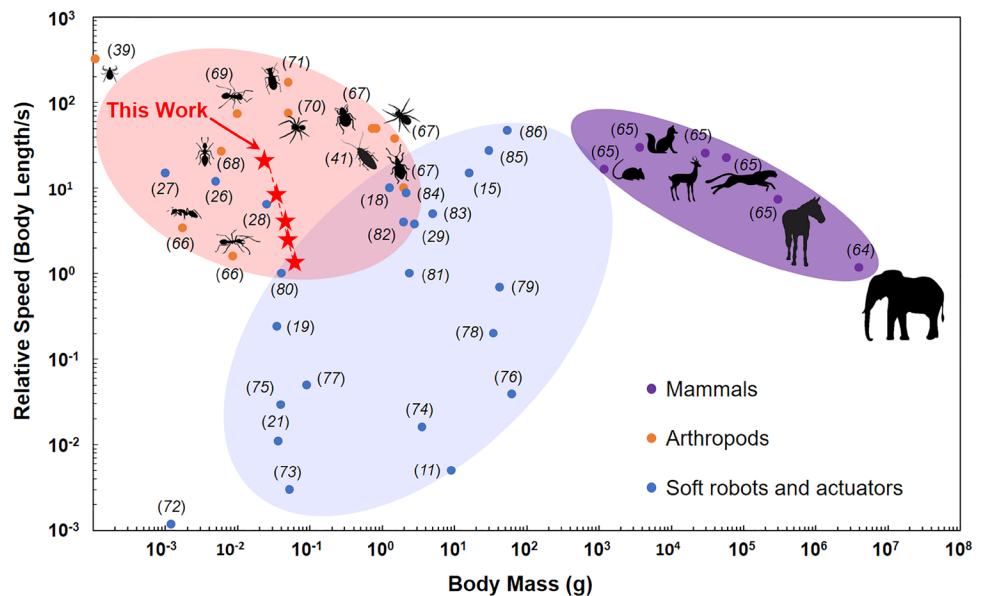

Fig. 4. Relative running speeds of some mammals, arthropods, soft robots, and actuators versus body mass. For animals including both mammals (purple) and arthropods (orange), relative speeds show a strong negative scaling law with respect to the body mass, showing that relative running speeds increase as body masses decrease. However, for soft robots, the relationship appears to be the opposite, where the relative running speeds decrease as the body mass decrease. The performances of the prototype robots (red stars with body lengths from 30 to 10 mm) follow a scaling law similar to that of living animals: Higher relative running speed was attained as the body mass decreased, with the fastest measured running speed at 20 BL/s among reported insect-scale robots and actuators (blue). For data, see table S3.

(45). Using a prototype 30-mm-long robot operating at 140 Hz as an example, we measured the voltage and current simultaneously using a data acquisition system for five cycles (fig. S10). The power consumption could be estimated as 0.343 mW by the integral of the voltage-current measurement results. When the robot operated near its resonant frequency, the cost of transport (COT) of the robot was about 14 (section S5), the lowest reported COT for robots and insects below 1 g (fig. S11) (46–59) with a relative speed of 4 BL/s under a power of 0.343 mW.

The comparison of relative moving speed

The relative moving speed is very important for animals because they often depend on fast locomotion to hunt for food, escape from predators, and/or compete for mating partners (60, 61). Researchers have shown that animals with high relative speeds are less likely to be caught and that relative speed may be more "ecologically relevant" than the absolute speed in various performance characterizations (61, 62). Figure 4 shows a comparison of relative running speeds with respect to body weights including our robots (red stars) and living animals, such as terrestrial mammals (purple) and running arthropods (orange), along with reported artificial soft robots or actuators (blue). For mammals, the trend in the elliptical and purple color shaded area indicates that the relative speed decreases as the body mass increases due to the scaling of mechanical constraints on the locomotive performance (61). However, small-size arthropods outperform larger animals in terms of their relative moving speeds. For example, a small mite, *Paratarsotomus macropalpis*, is now the world's fastest known running animal, with a relative speed at several hundred body lengths per second (39). An opposite trend exists for soft robots, as shown in the elliptical and blue color shaded area, which

suggests that the relative speed increases as the body mass increases (*19*) except for recent robots driven by an external magnetic force (*26–28*). The robots presented in this work (five red stars with the body lengths from 30 to 10 mm; Fig. 4) have sizes similar to those of arthropods with a similar performance trend where the relative speed increases as the body mass decreases. As discussed in section S4, the relative running speed of our prototype robots had a positive correlation with the resonant frequency, so our smaller robots operated at higher resonant frequencies to achieve faster relative running speeds. The working efficiency of our prototype robot is high because the simple structure contains no redundant energy-consuming components. Although some soft robots driven by magnetic fields, humidity, or heat or light sources can have fast instantaneous running speeds, slow responses and a bulky setup to generate the external power, such as the magnetic field, are among the limitations.

Robustness

Robustness is essential for the survival of animals displaying both fail-safe and fault-tolerant behavior. For example, a cockroach can withstand a load 900 times its own body weight without injury because of its soft and shape-changing exoskeleton (*37*). The robot presented here also has exceptional robustness characteristics resulting from the assembly of soft materials with simple structures. Experimentally, the robustness of the prototype soft robot was demonstrated by applying a 100-g mass (1500 times its own body weight) with little change in its speed after the mass was removed, as shown in movie S7. Moreover, the soft robot could continue to function (one-half of the original speed) after being stepped on by an adult human (59.5 kg), a load about 1 million times its own body weight (Fig. 5, A to C, and movie S7). We systematically tested the robust performance of a 3 cm–by–1.5 cm prototype robot (fig. S12). The prototype robot was driven with the same condition (200 V and 140 Hz) before and after the applied load. In fig. S12, we report the speeds of a prototype robot after applying and removing different loads with magnitudes ranging from 10 to 59,500 g. We define the compressibility as the ratio of the vertical height change to the original height of the robot. We observed that if the applied load is below 100 g, then the robot can recover back to the original shape and maintain greater than 88% of its original speed. As the applied load increased, the moving speed decreased. When the applied load was above 10 kg, the compressibility of the robot increased and saturated at about 0.95, while the speed reduced and saturated at near 50% of the original speed. Even under heavy applied loads that flatten the robot initially, the robot could still partially recover after the removal of the applied load.
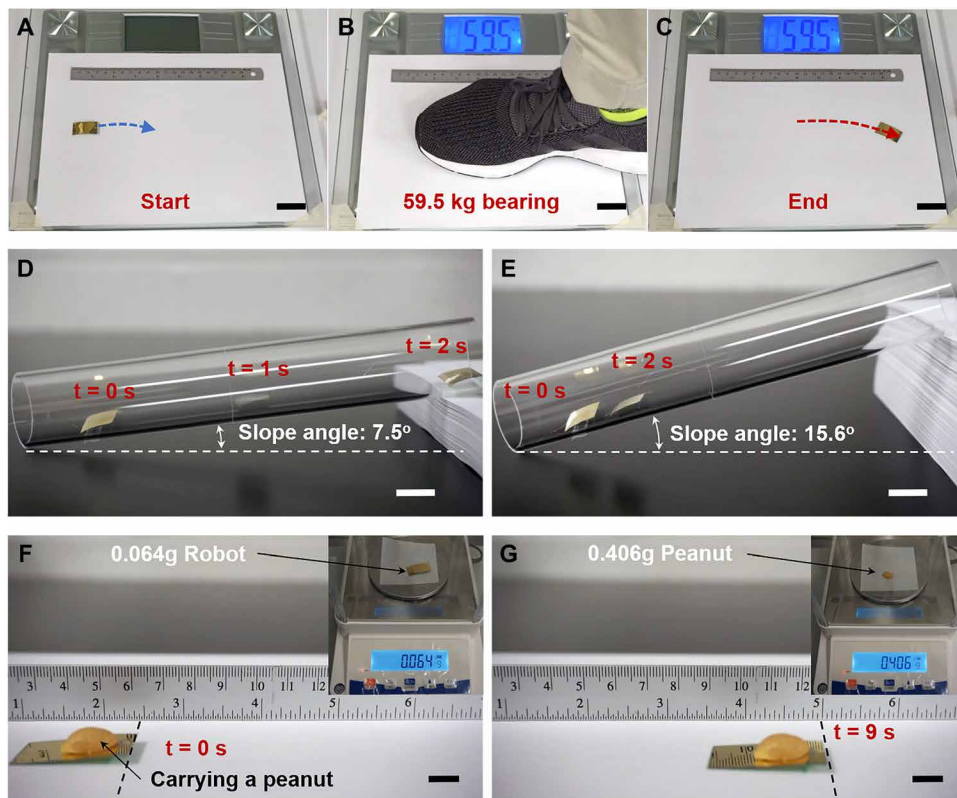

Fig. 5. Weight-bearing, slope-climbing, and load-carrying capabilities. (**A** to **C**) Soft robot can continue to function (one-half of the original speed) after being stepped on by an adult human (59.5 kg), a load about 1 million times its own body weight. Scale bars, 3 cm. A robot climbs a slope (**D**) of 7.5° with a relative speed of 7 BL/s and a slope (**E**) of 15.6° with a relative speed of 1 BL/s. Scale bars, 1 cm. (**F** and **G**) A robot (0.064 g) carries a peanut (0.406 g), which is six times its own body weight, to show the load-carrying capability. The speed with the peanut on top is about one-sixth of the original speed without the peanut. Scale bars, 1 cm.

Climbing and carrying loads

Animals and robots often need to do work such as climbing and carrying loads. The slope climbing capability of the robot is demonstrated in movie S7, in which the robot reached 7 BL/s while climbing a slope with an angle of 7.5° (Fig. 5D) and 1 BL/s while climbing a slope with an angle of 15.6° (Fig. 5E). Our soft prototype robot could also carry loads equal to the weight of a peanut (0.406 g) (Fig. 5, F and G). The robot was able to move smoothly while carrying a load that is six times its own weight at about one-sixth of the original speed (movie S7).

Speed enhancement by galloping-like gait

To further increase the running speed, we added and attached a back leg to a 3 cm–by–5 cm prototype robot to emulate galloping-like gaits (movie S8). Galloping is used by some rapid running mammals, where back bending increases stride length and allows the recovery of stored elastic energy (*63*). Specifically shown in (i) to (xi) of Fig. 6A, successive stages in a galloping stride and their corresponding schematic diagrams illustrate the operation of the galloping gait. With the more effective galloping-like gait mechanism, a two-legged robot achieved a running speed about three times that of a one-legged 3 cm–by–1.5 cm robot under similar driving conditions, as shown in movie S9. To investigate quantitative details, we show (Fig. 6B) the statistical duty cycles of various postures

between the one-legged and two-legged robots. We found that the prototype two-legged robot had longer aerial duty cycles (75% versus 51%) to boost the running speed.

Fig. 6. Galloping-like gait with the design of a two-legged robot. (**A**) Series of optical images (top) from the high-speed camera to show the galloping strides and their corresponding schematic diagrams (bottom). (**B**) Comparison of one-legged and two-legged robots in duty cycles in different operation postures. Error bars indicate mean ± 1 SD. See movie S9.

CONCLUSION

By generalizing several solutions found in animals, we introduce a fast and ultrarobust insect-scale soft robot for potential applications in environmental exploration, structural inspection, information reconnaissance, and disaster relief. Our robot uses the large vibration amplitude and a bouncing gait mechanism to generate a wavelike locomotion near its resonant frequency. Our prototype robot achieved a maximum relative speed of 20 BL/s, which is comparable with those of fast-moving arthropods and is faster than those of currently reported insect-scale robots. Furthermore, the robot can function with a low voltage supply of only 8 V, which demonstrates promise for the further integration of onboard circuits for future untethered operations. The scaling trend from the tested robots shows that miniaturization with higher resonant frequencies could further increase the relative speeds, but precision fabrication, the requirement of powering wires, and untethered operations could be the key challenges in pursuing smaller-scale robots. The working mechanism and structure of the robots presented here also show exceptional robustness in weight-bearing, slope-climbing, and load-carrying performances. The control of the robot's movement direction is another important next step. One simple way to turn would be to assemble two separated electrical domains, as shown in figs. S13 and S14 and movie S10. Driving signals (frequency, amplitude, or phase) of the two domains are controlled independently so that each of them allows different ground reaction forces to turn in the desired direction. By assembling domains with different sizes or shapes, a robot could add further maneuverability. Hence, we hope the proposed insect-scale robot paves a way to pursue fast and robust robots for practical applications.

MATERIALS AND METHODS

The prototype robot consists of a curved unimorph structure and a folded leg assembled with a simple process. The unimorph structure uses an 18-μm-thick PVDF film (PolyK Technologies, LLC) on top as the active layer and a 50-μm-thick PET tape (Gizmo Dorks) at the bottom as the inactive layer (25-μm-thick adhesive silicone and 25-μm-thick PET). The fabrication and assembly processes of a prototype robot are shown in fig. S15. To pattern electrodes on both sides of a PVDF film, we used a 2-mm-thick acrylic board (Soto Laser Cutting) patterned by laser as a shadow mask. The electrode consists of 10-nm-thick Pd and 40-nm-thick Au. The PVDF film was precisely cut with margins along the patterned electrodes by a pro-
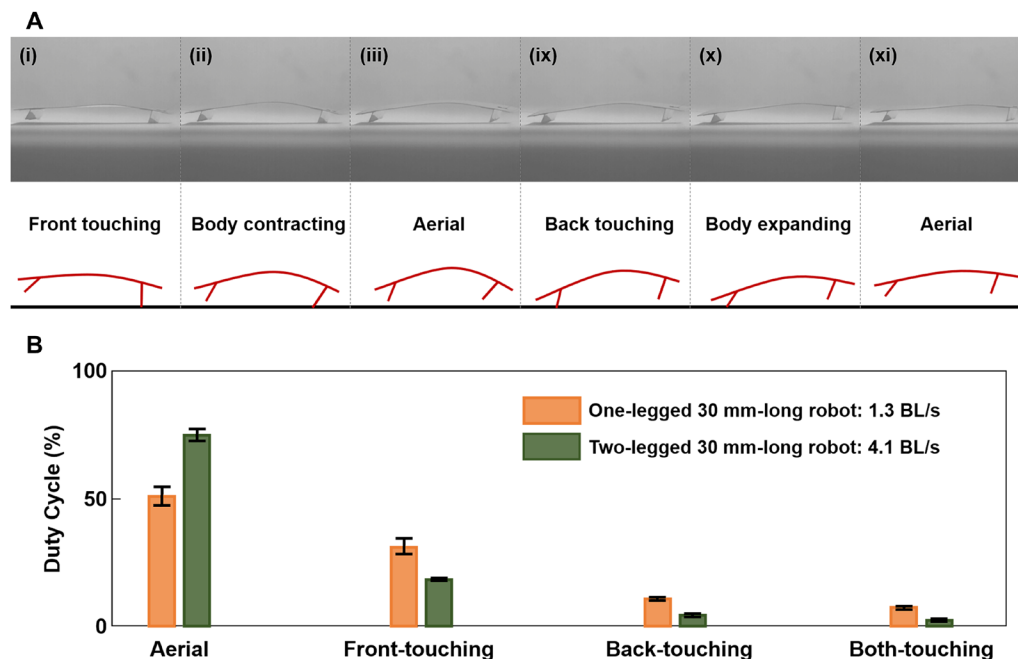
grammable paper-cutting machine (Silhouette America). Then, the PET tape with the same dimensions as the PVDF film was cut the same way. Two wires (Aluminium/Silicon Alloy, Custom Chip Connections) with a diameter of 25.4 μm were attached by aluminum tape on each side of the electrodes, serving as connections between the robot and external power supply. Next, the PVDF film and the PET tape were laminated together on top of a three-dimensional printed curved mold to form a curved (45°) unimorph structure. Last, a PET tape was adhered to the bottom layer of the robot to serve as the front leg.

SUPPLEMENTARY MATERIALS

robotics.sciencemag.org/cgi/content/full/4/32/eaax1594/DC1
Section S1. Actuation mechanism of PVDF film and curved unimorph structure
Section S2. Qualitative analysis of the locomotion mechanism
Section S3. Simplified dynamic model for the robot's locomotion
Section S4. Resonant frequency evaluation
Section S5. COT calculation
Fig. S1. Actuating mechanism of PVDF film and curved unimorph structure.
Fig. S2. Locomotion performances inside a tube.
Fig. S3. Conceptual image of the free body diagram: A robot at a both-touching posture.
Fig. S4. Velocity and force analysis for front-leg touchdown.
Fig. S5. System configurations of the simplified dynamic model.
Fig. S6. Gait statistics near fast speed.
Fig. S7. The relationship between robot length and resonant frequency for FEM simulation results under different boundary conditions compared with that of experimental results.
Fig. S8. Dynamic tests when the robot is clamped at one end.
Fig. S9. Locomotion of a robot under low driving voltage.
Fig. S10. Measurement of electrical parameters.
Fig. S11. COT of select robots (circles) and insects (squares) plotted against their body masses.
Fig. S12. Performance of a 3 cm–by–1.5 cm prototype robot after applying and removing different loads.
Fig. S13. Fabrication processes of a prototype robot with the turning ability.
Fig. S14. Direction control.
Fig. S15. Main fabrication and assembly processes of a prototype robot.
Table S1. Material parameters.

REFERENCES AND NOTES

1. M. Calisti, G. Picardi, C. Laschi, Fundamentals of soft robot locomotion. *J. R. Soc. Interface* **14**, 20170101 (2017).

2. D. Rus, M. T. Tolley, Design, fabrication and control of soft robots. *Nature* **521**, 467–475 (2015).

3. S. I. Rich, R. J. Wood, C. Majidi, Untethered soft robotics. *Nat. Electron.* **1**, 102–112 (2018).

4. S. Kim, C. Laschi, B. Trimmer, Soft robotics: A bioinspired evolution in robotics. *Trends Biotechnol.* **31**, 287–294 (2013).

5. J. Aguilar, T. Zhang, F. Qian, M. Kingsbury, B. McInroe, N. Mazouchova, C. Li, R. Maladen, C. Gong, M. Travers, R. L. Hatton, H. Choset, P. B. Umbanhowar, D. I. Goldman, A review on locomotion robophysics: The study of movement at the intersection of robotics, soft matter and dynamical systems. *Rep. Prog. Phys.* **79**, 110001 (2016).

6. Y. O. Aydin, J. M. Rieser, C. M. Hubicki, W. Savoie, D. I. Goldman, Physics approaches to natural locomotion: Every robot is an experiment, in *Robotic Systems and Autonomous Platforms* (Woodhead Publishing, 2019), pp. 109–127.

7. A. Rafsanjani, Y. Zhang, B. Liu, S. M. Rubinstein, K. Bertoldi, Kirigami skins make a simple soft actuator crawl. *Sci. Robot.* **3**, eaar7555 (2018).

8. W. Wang, J.-Y. Lee, H. Rodrigue, S.-H. Song, W.-S. Chu, S.-H. Ahn, Locomotion of inchworm-inspired robot made of smart soft composite (SSC). *Bioinspir. Biomim.* **9**, 046006 (2014).

9. K. Jung, J. C. Koo, J.-d. Nam, Y. K. Lee, H. R. Choi, Artificial annelid robot driven by soft actuators. *Bioinspir. Biomim.* **2**, S42–S49 (2007).

10. S. A. Rios, A. J. Fleming, Y. K. Yong, Miniature resonant ambulatory robot. *IEEE Robot. Autom. Lett.* **2**, 337–343 (2017).

11. B. Kim, M. G. Lee, Y. P. Lee, Y. Kim, G. Lee, An earthworm-like micro robot using shape memory alloy actuator. *Sens. Actuators A Phys.* **125**, 429–437 (2006).

12. D. W. Haldane, M. M. Plecnik, J. K. Yim, R. S. Fearing, Robotic vertical jumping agility via series-elastic power modulation. *Sci. Robot.* **1**, eaag2048 (2016).

13. N. Kagawa, H. Kazerooni, Biomimetic small walking machine, in *Proceedings of the 2001 IEEE/ IEEE/ASME International Conference on Advanced Intelligent Mechatronics*, Como, Italy, 8 to 12 July 2001 (IEEE, 2001).

14. K. L. Hoffman, R. J. Wood, Turning gaits and optimal undulatory gaits for a modular centipede-inspired millirobot, in *Proceedings of the 4th IEEE RAS/EMBS International Conference on Biomedical Robotics and Biomechatronics*, Roma, Italy, 24 to 27 June 2012 (IEEE, 2012).

15. P. Birkmeyer, K. Peterson, R. S. Fearing, DASH: A dynamic 16g hexapedal robot, in *Proceedings of the 2009 IEEE/RSJ International Conference on Intelligent Robots and Systems*, St. Louis, MO, 11 to 15 October 2009 (IEEE, 2009).

16. U. Saranli, M. Buehler, D. E. Koditschek, RHex: A simple and highly mobile hexapod robot. *Int. J. Rob. Res.* **20**, 616–631 (2016).

17. S. Kim, J. E. Clark, M. R. Cutkosky, iSprawl: Design and tuning for high-speed autonomous open-loop running. *Int. J. Rob. Res.* **25**, 903–912 (2006).

18. A. T. Baisch, O. Ozcan, B. Goldberg, D. Ithier, R. J. Wood, High speed locomotion for a quadrupedal microrobot. *Int. J. Rob. Res.* **33**, 1063–1082 (2014).

19. B. Shin, J. Ha, M. Lee, K. Park, G. H. Park, T. H. Choi, K.-J. Cho, H.-Y. Kim, Hygrobot: A self-locomotive ratcheted actuator powered by environmental humidity. *Sci. Robot.* **3**, eaar2629 (2018).

20. S.-W. Lee, J. H. Prosser, P. K. Purohit, D. Lee, Bioinspired hygromorphic actuator exhibiting controlled locomotion. *ACS Macro Lett.* **2**, 960–965 (2013).

21. Y. Ma, Y. Zhang, B. Wu, W. Sun, Z. Li, J. Sun, Polyelectrolyte multilayer films for building energetic walking devices. *Angew. Chem. Int. Ed.* **123**, 6378–6381 (2011).

22. E. Wang, M. S. Desai, S.-W. Lee, Light-controlled graphene-elastin composite hydrogel actuators. *Nano Lett.* **13**, 2826–2830 (2013).

23. M. Rogóż, H. Zeng, C. Xuan, D. S. Wiersma, P. Wasylczyk, Light-driven soft robot mimics caterpillar locomotion in natural scale. *Adv. Optic. Mater.* **4**, 1689–1694 (2016).

24. S.-J. Park, M. Gazzola, K. S. Park, S. Park, V. Di Santo, E. L. Blevins, J. U. Lind, P. H. Campbell, S. Dauth, A. K. Capulli, F. S. Pasqualini, S. Ahn, A. Cho, H. Yuan, B. M. Maoz, R. Vijaykumar, J.-W. Choi, K. Deisseroth, G. V. Lauder, L. Mahadevan, K. K. Parker, Phototactic guidance of a tissue-engineered soft-robotic ray. *Science* **353**, 158–162 (2016).

25. N. Cheng, G. Ishigami, S. Hawthorne, H. Chen, M. Hansen, M. Telleria, R. Playter, K. Iagnemma, Design and analysis of a soft mobile robot composed of multiple thermally activated joints driven by a single actuator, in *Proceedings of the 2010 IEEE International Conference on Robotics and Automation*, Anchorage, AK, 3 to 8 May 2010 (IEEE, 2010).

26. W. Hu, G. Z. Lum, M. Mastrangeli, M. Sitti, Small-scale soft-bodied robot with multimodal locomotion. *Nature* **554**, 81–85 (2018).

27. R. St. Pierre, W. Gosrich, S. Bergbreiter, A 3D-printed 1mg legged microrobot running at 15 body lengths per second, paper presented at Solid-State Sensors, Actuators, and Microsystems Workshop, Hilton Head, SC, 3 to 7 June 2018.

28. D. Vogtmann, R. S. Pierre, S. Bergbreiter, A 25mg magnetically actuated microrobot walking at > 5 body lengths/sec, *Proceedings of the 2018 IEEE International Conference on Micro Electro Mechanical Systems (MEMS),* Las Vegas, NV, 22 to 26 January 2017 (IEEE, 2017).

29. B. Goldberg, R. Zufferey, N. Doshi, E. F. Helbling, G. Whittredge, M. Kovac, R. J. Wood, Power and control autonomy for high-speed locomotion with an insect-scale legged robot. *IEEE Trans. Robot. Autom.* **3**, 987–993 (2018).

30. N. Lobontiu, M. Goldfarb, E. Garcia, A piezoelectric-driven inchworm locomotion device. *Mech. Mach. Theory* **36**, 425–443 (2001).

31. H. H. Hariri, L. A. Prasetya, S. Foong, G. S. Soh, K. N. Otto, K. L. Wood, A tether-less legged piezoelectric miniature robot using bounding gait locomotion for bidirectional motion, in *Proceedings of the 2016 IEEE International Conference on Robotics and Automation,* Stockholm, Sweden, 16 to 21 May 2016 (IEEE, 2016).

32. Y. Wu, K. Y. Ho, K. Kariya, R. Xu, W. Cai, J. Zhong, Y. Ma, M. Zhang, X. Wang, L. Lin, Pre-curved PVDF/PI unimorph structures for biomimic soft crawling actuators, *Proceedings of the 2018 IEEE International Conference on Micro Electro Mechanical Systems (MEMS)*, Belfast, UK, 21 to 25 January 2018 (IEEE, 2018).

33. P. Xiao, N. Yi, T. Zhang, Y. Huang, H. Chang, Y. Yang, Y. Zhou, Y. Chen, Construction of a fish-like robot based on high performance graphene/PVDF bimorph actuation materials. *Adv. Sci.* **3**, 1500438 (2016).

34. L. Hines, K. Petersen, G. Z. Lum, M. Sitti, Soft actuators for small-scale robotics. *Adv. Mater.* **29**, 1603483 (2017).

35. G. Z. Yang, J. Bellingham, P. E. Dupont, P. Fischer, L. Floridi, R. Full, N. Jacobstein, V. Kumar, M. McNutt, R. Merrifield, B. J. Nelson, B. Scassellati, M. Taddeo, R. Taylor, M. Veloso, Z. L. Wang, R. Wood, The grand challenges of Science Robotics. *Sci. Robot.* **3**, eaar7650 (2018).

36. M. H. Dickinson, C. T. Farley, R. J. Full, M. A. R. Koehl, R. Kram, S. Lehman, How animals move: An integrative view. *Science* **288**, 100–106 (2000).

37. K. Jayaram, R. J. Full, Cockroaches traverse crevices, crawl rapidly in confined spaces, and inspire a soft, legged robot. *Proc. Natl. Acad. Sci. U.S.A.* **113**, E950–E957 (2016).

38. R. J. Bomphrey, T. Nakata, N. Phillips, S. M. Walker, Smart wing rotation and trailing-edge vortices enable high frequency mosquito flight. *Nature* **544**, 92–95 (2017).

39. S. Rubin, M. H.-Y. Young, J. C. Wright, D. L. Whitaker, A. N. Ahn, Exceptional running and turning performance in a mite. *J. Exp. Biol.* **219**, 676–685 (2016).

40. G. C. Wu, J. C. Wright, D. L. Whitaker, A. N. Ahn, Kinematic evidence for superfast locomotory muscle in two species of teneriffiid mites. *J. Exp. Biol.* **213**, 2551–2556 (2010).

41. R. J. Full, M. S. Tu, Mechanics of a rapid running insect: Two-, four- and six-legged locomotion. *J. Exp. Biol.* **156**, 215–231 (1991).

42. B. K. Ahlborn, R. W. Blake, W. Megill, Frequency tuning in animal locomotion. *Fortschr. Zool.* **109**, 43–53 (2006).

43. M. H. Dickinson, M. S. Tu, The function of dipteran flight muscle. *Comp. Biochem. Physiol.* **116**, 223–238 (1997).

44. V. Wahl, S. E. Pfeffer, M. Wittlinger, Walking and running in the desert ant *Cataglyphis fortis*. *J. Comp. Physiol. A* **201**, 645–656 (2015).

45. G.-Y. Gu, J. Zhu, L.-M. Zhu, X. Zhu, A survey on dielectric elastomer actuators for soft robots. *Bioinspir. Biomim.* **12**, 011003 (2017).

46. R. St. Pierre, S. Bergbreiter, Toward autonomy in sub-gram terrestrial robots. *Annu. Rev. Control. Robot. Auton. Syst.* **2**, 231–252 (2019).

47. E. Y. Erdem, Y.-M. Chen, M. Mohebbi, J. W. Suh, G. T. A. Kovacs, R. B. Darling, K. F. Böhringer, Thermally actuated omnidirectional walking microrobot. *J. Microelectromech. Syst.* **19**, 433–442 (2010).

48. T. Ebefors, J. U. Mattsson, E. Kälvesten, G. Stemme, A walking silicon micro-robot, in *Proceedings of the 10th International Conference on Solid-State Sensors and Actuators: Transducers* (IEEE, 1999).

49. W. A. Churaman, L. J. Currano, C. J. Morris, J. E. Rajkowski, S. Bergbreiter, The first launch of an autonomous thrust-driven microrobot using nanoporous energetic silicon. *J. Microelectromech. Syst.* **21**, 198–205 (2012).

50. M. Qi, Y. Zhu, Z. Liu, X. Zhang, X. Yan, L. Lin, A fast-moving electrostatic crawling insect, in *Proceedings of the 2018 IEEE International Conference on Micro Electro Mechanical Systems (MEMS)*, Las Vegas, NV, 22 to 26 January 2017 (IEEE, 2017).

51. S. Hollar, A. Flynn, C. Bellew, K. Pister, Solar powered 10 mg silicon robot, in *Sixteenth Annual International Conference on Micro Electro Mechanical Systems* (IEEE, 2003).

52. J. T. Greenspun, K. Pister, First leaps of an electrostatic inchwormmotor-driven jumping microrobot, in *Hilton Head Solid-State Sensors, Actuators, and Microsystems Workshop*, Hilton Head Island, SC, 3 to 7 June 2018.

53. D. Berrigan, J. R. Lighton, Bioenergetic and kinematic consequences of limblessness in larval Diptera. *J. Exp. Biol.* **179**, 245–259 (1993).

54. T. F. Jensen, I. Holm-Jensen, Energetic cost of running in workers of three ant species, *Formica fusca* L., *Formica rufa* L., and *Camponotus herculeanus* L. (Hymenoptera, Formicidae). *J. Comp. Physiol.* **137**, 151–156 (1980).

55. J. R. B. Lighton, G. A. Bartholomew, D. H. Feener, Energetics of locomotion and load carriage and a model of the energy cost of foraging in the leaf-cutting Ant *Atta colombica* Guer. *Physiol. Zool.* **60**, 524–537 (1987).

56. W. Driesen, A. Rida, J. Breguet, R. Clavel, Friction based locomotion module for mobile MEMS robots, in *2007 IEEE/RSJ International Conference on Intelligent Robots and Systems* (IEEE, 2007).

57. L. Reinhardt, R. Blickhan, Level locomotion in wood ants: Evidence for grounded running. *J. Exp. Biol.* **217**, 2358–2370 (2014).

58. D. S. Contreras, D. S. Drew, K. S. J. Pister, First steps of a millimeter-scale walking silicon robot, in *IEEE 19th International Conference on Solid-State Sensors, Actuators and Microsystems (Transducers'17)* (IEEE, 2017).

59. J. H. Fewell, J. F. Harrison, J. R. B. Lighton, M. D. Breed, Foraging energetics of the ant, *Paraponera clavata*. *Oecologia* **105**, 419–427 (1996).

60. M. R. Hirt, W. Jetz, B. C. Rall, U. Brose, A general scaling law reveals why the largest animals are not the fastest. *Nat. Ecol. Evol.* **1**, 1116–1122 (2017).

61. J. Iriarte-Díaz, Differential scaling of locomotor performance in small and large terrestrial mammals. *J. Exp. Biol.* **205**, 2897–2908 (2002).

62. R. Van Damme, T. J. M. Van Dooren, Absolute versus per unit body length speed of prey as an estimator of vulnerability to predation. *Anim. Behav.* **57**, 347–352 (1999).

63. R. M. Alexander, N. J. Dimery, R. F. Ker, Elastic structures in the back and their role in galloping in some mammals. *J. Zool.* **207**, 467–482 (1985).

64. R. M. Alexander, Allometry of the limbs of antelopes (Bovidae). *J. Zool.* **183**, 125–146 (1977).

65. R. M. Alexander, V. A. Langman, A. S. Jayes, Fast locomotion of some African ungulates. *J. Zool.* **183**, 291–300 (1977).

66. F. D. Duncan, R. M. Crewe, A comparison of the energetics of foraging of three species of *Leptogenys* (Hymenoptera, Formicidae). *Physiol. Entomol.* **18**, 372–378 (1993).

67. G. A. Bartholomew, J. R. B. Lighton, G. N. Louw, Energetics of locomotion and patterns of respiration in tenebrionid beetles from the Namib Desert. *J. Comp. Physiol. B* **155**, 155–162 (1985).

68. A. H. Hurlbert, F. Ballantyne, S. Powell, Shaking a leg and hot to trot: The effects of body size and temperature on running speed in ants. *Ecol. Entomol.* **33**, 144–154 (2008).

69. M. Wittlinger, R. Wehner, H. Wolf, The desert ant odometer: A stride integrator that accounts for stride length and walking speed. *J. Exp. Biol.* **210**, 198–207 (2007).

70. C. C. Amaya, P. D. Klawinski, D. R. Formanowicz Jr., The effects of leg autotomy on running speed and foraging ability in two species of wolf spider, (Lycosidae). *Am. Midl. Nat.* **145**, 201–205 (2001).

71. S. Kamoun, S. A. Hogenhout, Flightlessness and rapid terrestrial locomotion in tiger beetles of the Cicindela L. Subgenus Rivacindela van Nidek from saline habitats of Australia (Coleoptera: Cicindelidae). *Coleopts. Bull.* **50**, 221–230 (1996).

72. S. Maeda, Y. Hara, T. Sakai, R. Yoshida, S. Hashimoto, Self-walking gel. *Adv. Mater.* **19**, 3480–3484 (2007).

73. D. Morales, E. Palleau, M. D. Dickey, O. D. Velev, Electro-actuated hydrogel walkers with dual responsive legs. *Soft Matter* **10**, 1337–1348 (2014).

74. N. Tomita, K. Takagi, K. Asaka, Development of a quadruped soft robot with fully IPMC body, in *Proceedings of the 2011 SICE Annual Conference*, Tokyo, Japan, 13 to 18 September 2011 (SICE, 2011).

75. H. Lu, M. Zhang, Y. Yang, Q. Huang, T. Fukuda, Z. Wang, Y. Shen, A bioinspired multilegged soft millirobot that functions in both dry and wet conditions. *Nat. Commun.* **9**, 3944–3950 (2018).

76. S. W. Kwok, S. A. Morin, B. Mosadegh, J.-H. So, R. F. Shepherd, R. V. Martinez, B. Smith, F. C. Simeone, A. A. Stokes, G. M. Whitesides, Magnetic assembly of soft robots with hard components. *Adv. Funct. Mater.* **24**, 2180–2187 (2014).

77. L. Xu, H.-Q. Chen, J. Zou, W.-T. Dong, G.-Y. Gu, L.-M. Zhu, X.-Y. Zhu, Bio-inspired annelid robot: A dielectric elastomer actuated soft robot. *Bioinspir. Biomim.* **12**, 025003 (2017).

78. C. T. Nguyen, H. Phung, T. D. Nguyen, H. Jung, H. R. Choi, Multiple-degrees-of-freedom dielectric elastomer actuators for soft printable hexapod robot. *Sens. Actuators A Phys.* **267**, 505–516 (2017).

79. T. Li, G. Li, Y. Liang, T. Cheng, J. Dai, X. Yang, B. Liu, Z. Zeng, Z. Huang, Y. Luo, T. Xie, W. Yang, Fast-moving soft electronic fish. *Sci. Adv.* **3**, e1602045 (2017).

80. M. Duduta, D. R. Clarke, R. J. Wood, A high speed soft robot based on dielectric elastomer actuators, in *Proceedings of the 2017 IEEE International Conference on Robotics and Automation* (IEEE, 2017), Singapore, 29 May to 3 June 2017.

81. A. M. Hoover, E. Steltz, R. S. Fearing, RoACH: An autonomous 2.4g crawling hexapod robot, in *Proceedings of the 2008 IEEE/RSJ International Conference on Intelligent Robots and Systems* (IEEE, 2008), Nice, France, 22 to 26 September 2008.

82. A. T. Baisch, P. S. Sreetharan, R. J. Wood, Biologically-inspired locomotion of a 2g hexapod robot, in *Proceedings of the 2010 IEEE/RSJ International Conference on Intelligent Robots and Systems* (IEEE, 2010), Taipei International Convention Center, Taipei, Taiwan, 18 to 22 October 2010.

83. H.-T. Lin, G. G. Leisk, B. Trimmer, GoQBot: A caterpillar-inspired soft-bodied rolling robot. *Bioinspir. Biomim.* **6**, 026007 (2011).

84. S.-i. Aoshima, T. Tsujimura, T. Yabuta, A miniature mobile robot using piezo vibration for mobility in a thin tube. *J. Dyn. Syst. Meas. Control* **115**, 270–278 (1993).

85. D. W. Haldane, K. C. Peterson, F. L. Garcia Bermudez, R. S. Fearing, Animal-inspired design and aerodynamic stabilization of a hexapedal millirobot, in *Proceedings of the 2013 IEEE International Conference on Robotics and Automation* (IEEE, 2013), Karlsruhe, Germany, 6 to 10 May 2013.

86. D. W. Haldane, R. S. Fearing, Running beyond the bio-inspired regime, in *Proceedings of the 2015 IEEE International Conference on Robotics and Automation* (IEEE, 2015), Washington, USA, 26 to 30 May 2015.

87. C.-H. Hsueh, Modeling of elastic deformation of multilayers due to residual stresses and external bending. *J. Appl. Phys.* **91**, 9652–9656 (2002).

Citation: Y. Wu, J. K. Yim, J. Liang, Z. Shao, M. Qi, J. Zhong, Z. Luo, X. Yan, M. Zhang, X. Wang, R. S. Fearing, R. J. Full, L. Lin, Insect-scale fast moving and ultrarobust soft robot. *Sci. Robot.* **4**, eaax1594 (2019).

Science Robotics

Insect-scale fast moving and ultrarobust soft robot

Yichuan Wu, Justin K. Yim, Jiaming Liang, Zhichun Shao, Mingjing Qi, Junwen Zhong, Zihao Luo, Xiaojun Yan, Min Zhang, Xiaohao Wang, Ronald S. Fearing, Robert J. Full and Liwei Lin

ARTICLE TOOLS	http://robotics.sciencemag.org/content/4/32/eaax1594
SUPPLEMENTARY MATERIALS	http://robotics.sciencemag.org/content/suppl/2019/07/26/4.32.eaax1594.DC1
REFERENCES	This article cites 66 articles, 11 of which you can access for free http://robotics.sciencemag.org/content/4/32/eaax1594#BIBL
PERMISSIONS	http://www.sciencemag.org/help/reprints-and-permissions

Use of this article is subject to the Terms of Service